JACS
JOURNAL OF THE AMERICAN CHEMICAL SOCIETY
pubs.acs.org/JACS
Article

Surface-Clean Au_{25} Nanoclusters in Modulated Microenvironment Enabled by Metal–Organic Frameworks for Enhanced Catalysis

He Wang, Xiyuan Liu, Weijie Yang, Guangyang Mao, Zheng Meng, Zhikun Wu, and Hai-Long Jiang*

Cite This: J. Am. Chem. Soc. 2022, 144, 22008–22017

ABSTRACT: Metal nanoclusters (NCs) with atomically precise structures have sparked interest in catalysis. Unfortunately, their high aggregation tendency and the spatial resistance of surface ligands pose significant challenges. Herein, Au_{25} NCs are encapsulated into isoreticular metal–organic frameworks (MOFs), namely UiO-66-X (X = H, NH_2, OH, and NO_2), followed by the removal of surface ligands on Au_{25} NCs. The resulting surface-clean Au_{25} NCs, protected by the MOF spatial confinement, exhibit much superior activity and stability with respect to pristine Au_{25} NCs in the oxidative esterification of furfural. Remarkably, experimental and theoretical results jointly demonstrate that diverse functional groups on UiO-66-X modulate the Au_{25} electronic state, giving rise to the discriminated substrate adsorption energy of Au_{25}@UiO-66-X. As a result, the high electron density and suitable substrate adsorption ability dominate the activity trend: Au_{25}@UiO-66-NH_2 > Au_{25}@UiO-66-OH > Au_{25}@UiO-66 > Au_{25}@UiO-66-NO_2. This work develops a new strategy for the stabilization of surface-clean metal NCs in pore wall-engineered MOFs for enhanced catalysis.

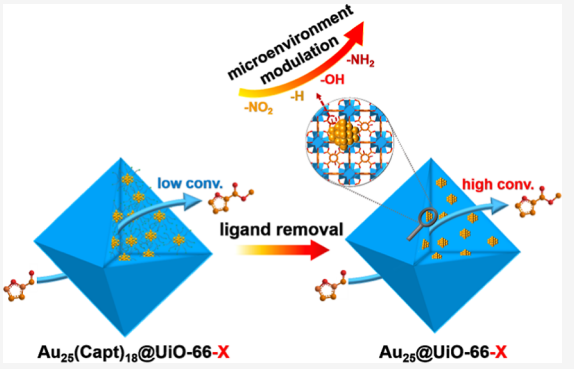

INTRODUCTION

Catalysis lays the foundation of the modern chemical industry and is critical to the advancement of human life and society. Supported metal catalysts are widely employed in industrial catalysis.[1−3] In these catalysts, metal nanoparticles (NPs) are usually prepared with size distributions in a certain range, which reflects their inhomogeneous structures and limits the catalytic performance, thereby providing insights into the underlying mechanism. Recently, atomically precise metal nanoclusters (NCs) have experienced rapid development, opening up new opportunities for the precise fabrication of supported catalysts.[4−7] Metal NCs feature tiny and uniform sizes, identical active sites, and unique geometric and electronic structures, making them highly reactive in a variety of reactions.[8−10] Unfortunately, the steric hindrance of surface ligands and the high tendency to aggregation severely affect their catalytic activity.[11] Intuitively, it is necessary to expose more active sites by removing the surface ligands of metal NCs.[12−14] However, substantial aggregation readily occurs upon surface ligand removal, inevitably reducing their catalytic activity. On the other hand, the surface ligands not only stabilize metal NCs but also exert a significant impact on their catalytic behavior, as the metal NCs are very sensitive to their surroundings groups.[15−18] In this context, it is highly desirable to restrict their aggregation for enhanced catalysis by spatial confinement with porous matrices, the pore walls of which are readily decorated with functional groups to provide an optimized surrounding microenvironment for the confined metal NCs.

To meet the above requirements as a class of crystalline solids, metal–organic frameworks (MOFs), featuring high porosity and well-defined and tailorable structures, would be ideal candidates.[19−22] They have been recognized to be suitable hosts to stabilize metal NPs for synergistic catalysis.[23−30] Similar to metal NPs, metal NCs should be easily encapsulated into MOFs. It is possible to remove surface ligands from metal NCs encapsulated in MOFs,[31,32] generating ligand-free metal NCs stabilized in MOF pores. To date, although there have been several reports on the incorporation of metal NCs into MOFs in recent years,[33−37] the studies are simply limited to the function synergy between the two components, and the MOF contribution to the resulting catalytic performance has not been fully exploited. In fact, the MOF pore walls can be readily furnished with diverse functional groups, creating a modulated microenvironment around the encapsulated metal NCs. Although they are not bound to each other, these groups in close proximity to the metal sites, similar to the interactions in the binding pocket of enzymes, would have a significant impact on metal NCs by means of electron transfer, steric hindrance, weak interactions

Received: August 27, 2022
Published: November 21, 2022

https://doi.org/10.1021/jacs.2c09136
J. Am. Chem. Soc. 2022, 144, 22008–22017

Scheme 1. Illustration of the Synthetic Route to Surface-Clean Au_{25}@UiO-66 for Improved Catalysis Based on Microenvironment Modulation around Au_{25} by Furnishing Diverse Functional Groups on MOF Pore Walls

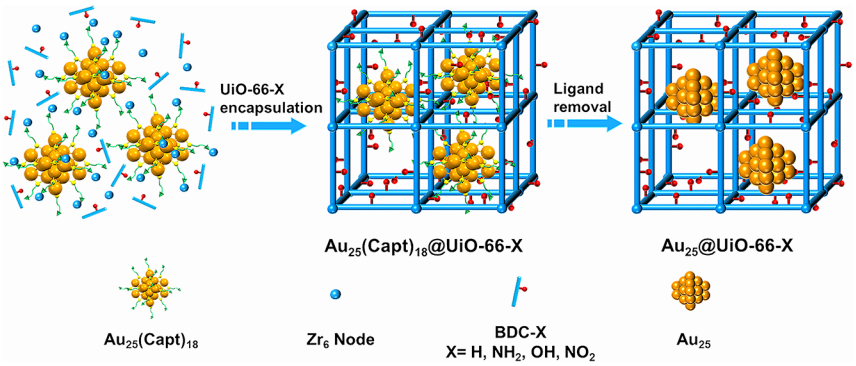

with substrates and intermediates, and so forth, leading to improved catalysis.[38−41] In this context, the removal of original surface ligands on the metal NCs is highly desired, as this would be not only beneficial to the aforementioned accessibility but also favorable to the creation of direct contact between the metal NCs and the MOF pore wall groups, thereby improving catalysis. Moreover, the resulting metal@MOF composites with a direct interface and readily tailorable structures would provide a relatively clear model for understanding the relationship of structure−performance in catalysis, which, to our knowledge, has yet been investigated.

In this work, representative isoreticular MOFs, UiO-66-X (X = H, NH_2, OH, and NO_2), are assembled onto atomically precise $Au_{25}(Capt)_{18}$ (Capt = captopril) based on electrostatic attraction and coordination interaction (Scheme 1). Upon removing the interfacial thiol ligands between $Au_{25}(Capt)_{18}$ and the MOFs, the aggregation of Au_{25} NCs is suppressed due to the spatial confinement induced by the MOFs. As expected, the resulting Au_{25}@UiO-66-X with surface-clean Au_{25} NCs exhibits much better activity than the pristine $Au_{25}(Capt)_{18}$ in the catalytic oxidative esterification of furfural. Remarkably, the electronic donation and withdrawal effects of the functional groups give rise to discriminated Au_{25} electronic states based on experimental and theoretical results, which are associated with differentiated substrate adsorption energies over Au_{25}@UiO-66-X. As a result, the modulated microenvironments around Au_{25} created by the diverse groups dangling on the MOF pore walls lead to distinctly different activities of Au_{25}@UiO-66-X, among which Au_{25}@UiO-66-NH_2 gives the highest activity in the oxidative esterification of furfural. By contrast, when the $Au_{25}(Capt)_{18}$ is supported on the MOF surface, their surface ligand removal induces migration and growth of Au_{25} under the same conditions, causing much reduced activity. As far as we know, this is the first demonstration that the spatial confinement and pore wall engineering of MOFs work synergistically for metal NCs toward enhanced catalysis.

RESULTS AND DISCUSSION

$Au_{25}(Capt)_{18}$ is selected as a representative NC as it possesses a stable structure and abundant carboxyl sites on the surface.[42] Its high purity has been jointly validated by the UV−vis spectrum, matrix-assisted laser desorption ionization time-of-flight mass spectrometry (MALDI-TOF-MS), and transmission electron microscopy (TEM) results (Figures S1 and S2). To avoid the structural damage of Au_{25} NCs at a high temperature during the encapsulation in solution, $Au_{25}(Capt)_{18}$ encapsulated into UiO-66, denoted $Au_{25}(Capt)_{18}$@UiO-66, was obtained via in situ self-assembly of Zr_6O_x clusters, $Au_{25}(Capt)_{18}$ NCs and benzene-1,4-dicarboxylate (BDC) at an ambient temperature.[43] The zeta potentials of $Au_{25}(Capt)_{18}$ and Zr_6O_x clusters in dimethylformamide (DMF) were measured to be −64.1 and +4.3 mV, respectively, guaranteeing their electrostatic attraction. Moreover, given a large number of negatively charged carboxyl groups on the surface, $Au_{25}(Capt)_{18}$ can be encapsulated inside UiO-66 by the self-assembly with cationic Zr_6O_x clusters or attached to the MOF outer surface by coordination and electrostatic interaction, affording $Au_{25}(Capt)_{18}$@UiO-66 and $Au_{25}(Capt)_{18}$/UiO-66, respectively.[44] Powder X-ray diffraction (XRD) patterns indicate that the spatial position of $Au_{25}(Capt)_{18}$ relative to UiO-66 has no influence on MOF crystallinity (Figure S3). The UV−vis diffuse reflectance spectra of $Au_{25}(Capt)_{18}$@UiO-66 and $Au_{25}(Capt)_{18}$/UiO-66 show characteristic absorption peaks of Au_{25} NCs at ∼670 nm, indicating that the structure of $Au_{25}(Capt)_{18}$ is inherited after the integration with UiO-66 (Figure S4). Nitrogen sorption results indicate that the Brunauer−Emmett−Teller (BET) surface area of $Au_{25}(Capt)_{18}$@UiO-66 (853 m^2/g) is much lower than that of $Au_{25}(Capt)_{18}$/UiO-66 (1174 m^2/g), the latter of which is very close to that of UiO-66 (1224 m^2/g) (Figure S5). The results reflect that the pore occupation of UiO-66 by $Au_{25}(Capt)_{18}$ is $Au_{25}(Capt)_{18}$@UiO-66, while $Au_{25}(Capt)_{18}$ might stay on the MOF surface for $Au_{25}(Capt)_{18}$/UiO-66. Moreover, no significant size change can be observed for $Au_{25}(Capt)_{18}$ in $Au_{25}(Capt)_{18}$@UiO-66 and $Au_{25}(Capt)_{18}$/UiO-66 by high-angle annular dark-field scanning TEM (HAADF-STEM) (Figure 1a,b). The energy-dispersive X-ray spectroscopy (EDS) mapping analyses reveal that Au species is uniformly dispersed in the MOF particle for $Au_{25}(Capt)_{18}$@UiO-66, while the Au is prone to distribute at the MOF edges in $Au_{25}(Capt)_{18}$/UiO-66 (Figures S6 and S7). By direct comparison of HAADF-STEM and secondary electron STEM (SE-STEM) images for the same particles, it is clear that $Au_{25}(Capt)_{18}$ NCs stay inside and on the external surface of the MOF, respectively, in $Au_{25}(Capt)_{18}$@UiO-66 and $Au_{25}(Capt)_{18}$/UiO-66 (Figure S8), verifying the location of $Au_{25}(Capt)_{18}$ NCs and in good agreement with the above N_2 sorption results.

The catalytic activity of $Au_{25}(Capt)_{18}$ is usually limited because its surface ligands impede the accessibility of the reactants to the active Au centers.[45−48] To remove the surface ligands, heat treatment might be a possible choice, but the specific temperature should be carefully selected to avoid the structural collapse of UiO-66.[49] Thermogravimetric analysis

https://doi.org/10.1021/jacs.2c09136
J. Am. Chem. Soc. 2022, 144, 22008−22017

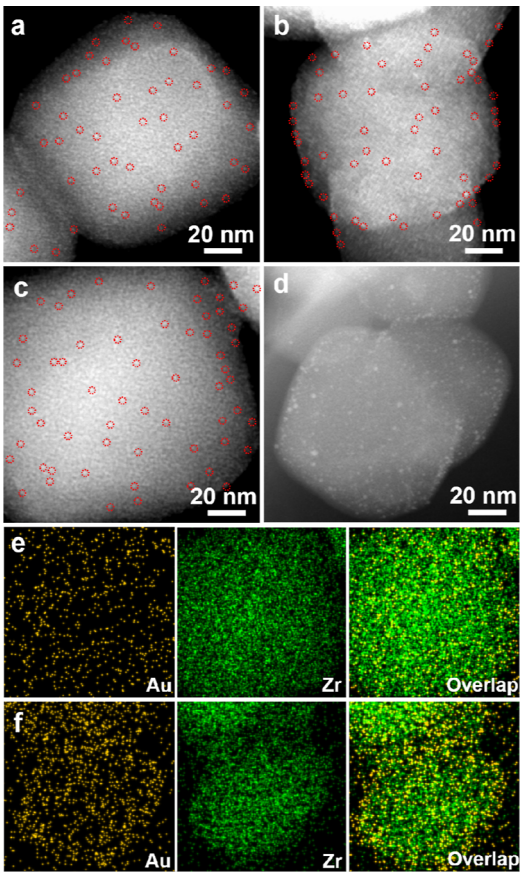

Figure 1. HAADF-STEM images of (a) $Au_{25}(Capt)_{18}$@UiO-66, (b) $Au_{25}(Capt)_{18}$/UiO-66, (c) Au_{25}@UiO-66, and (d) Au_{25}/UiO-66. EDS mapping of Au and Zr elements for (e) Au_{25}@UiO-66 and (f) Au_{25}/UiO-66. The tiny Au_{25} NCs are highlighted with red dashed circles.

(TGA) illustrates that the surface ligands of $Au_{25}(Capt)_{18}$ can be stripped off by heating above 250 °C (Figure S9). Therefore, both $Au_{25}(Capt)_{18}$@UiO-66 and $Au_{25}(Capt)_{18}$/UiO-66 are activated by heating at 275 °C for 3 h in a vacuum to ensure the structural integrity of UiO-66 while removing the surface ligands of Au_{25} NCs, respectively, yielding Au_{25}@UiO-66 and Au_{25}/UiO-66.

Powder XRD patterns demonstrate the well-maintained MOF crystallinity after the above heat treatment (Figure S3). HAADF-STEM images display that, while the size of Au_{25} encapsulated inside UiO-66 does not change after heat treatment (Figure 1c), significant agglomeration occurs to Au_{25} on the MOF outer surface (Figure 1d). The EDS mapping analyses and SE-STEM images illustrate that the spatial location of Au_{25} NCs relative to the MOF particle is not influenced after heat treatment (Figures 1e,f and S10). Nitrogen sorption suggests that Au_{25}@UiO-66 and Au_{25}/UiO-66 remain highly porous (Figure S11). Compared to $Au_{25}(Capt)_{18}$@UiO-66, the BET surface area increases to 1056 m^2/g for Au_{25}@UiO-66 due to the removal of Au_{25} surface ligands, while the BET surface area of Au_{25}/UiO-66 (1209 m^2/g) is close to $Au_{25}(Capt)_{18}$/UiO-66 (1174 m^2/g), which further supports the above affirmation of different Au spatial locations in these composites.

CO adsorption by diffuse reflectance infrared Fourier transform spectroscopy (CO-DRIFTS) indicates that no related CO adsorption peak can be observed for $Au_{25}(Capt)_{18}$@UiO-66 and $Au_{25}(Capt)_{18}$/UiO-66 possibly due to the blocked Au_{25} surface sites by ligands (Figures 2a and S12).[46] Upon heat treatment, intense CO adsorption peaks appear at 2109 and 2111 cm^{-1} for Au_{25}@UiO-66 and Au_{25}/UiO-66, respectively, which are assignable to the CO adsorption on Au^0, inferring the successful removal of the ligand from the Au_{25} surface.[50] The X-ray photoelectron spectroscopy (XPS) peak of S 2p disappears completely after heat treatment (Figures 2b and S13), which is consistent with the undetectable S content in the inductively coupled plasma atomic emission spectroscopy (ICP−AES) tests (Table S1). The XPS spectra of Au_{25}@UiO-66 and Au_{25}/UiO-66 show that the Au $4f_{7/2}$ peaks shift to lower binding energies upon removal of the ligand, close to that of metallic Au, which supports stripping off the strong electron-donated thiolate ligand (Figure 2c,d). All these results confirm that all captopril ligands are almost removed from the Au_{25} surface.

The ligand-free Au_{25} NCs confined in UiO-66 integrate the merits of uniform and tiny sizes as well as good accessibility of Au_{25} NCs, which prompts us to investigate their catalytic performance. Furfural is a widely applied biomass chemical, and its oxidative esterification to methyl 2-furoate (MF) is an important route to fragrance production in the fine chemical industry.[51] Efficient conversion of furfural in methanol to MF by green and sustainable one-pot oxidation is an ideal chemical process for value-added products.[52] Au_{25}@UiO-66 is believed to be very promising toward this process, as Au NPs have been described as excellent catalytic centers in previous reports.[53,54]

The experiments over a series of control catalysts have been conducted to understand the activity origin and critical issues in the catalytic system (Table 1). No product is detected in the presence of UiO-66 or the absence of catalyst (entries 1 and 2). When $Au_{25}(Capt)_{18}$, $Au_{25}(Capt)_{18}$@UiO-66, and $Au_{25}(Capt)_{18}$/UiO-66 are adopted, very low activity with furfural conversions of 3.5, 2.8, and 5.1%, respectively, is observed (entries 3−5). Strikingly, upon the surface ligand removal of Au_{25} NCs, incredibly increased activity with conversions up to 99.9 and 68.6% are achieved for Au_{25}@UiO-66 and Au_{25}/UiO-66, respectively (entries 6 and 7). The much enhanced activity is most likely attributed to the improved accessibility of Au sites. The apparently higher activity of Au_{25}@UiO-66 than that of Au_{25}/UiO-66 is assignable to the aggregation of Au_{25} on the MOF surface in the latter. It is found that the conversion of furfural gradually increases with prolonged reaction time until the reaction is completed, during which the reaction keeps high selectivity to MF (Figure S14). In addition, the activity of Au_{25}@UiO-66 is also higher than that of both Au_{25}/ZrO_2 (57.9%) and AuNPs@UiO-66 (62.4%) (entries 8 and 9). The superior activity of Au_{25}@UiO-66 is likely attributed to not only the high activity of Au_{25} NCs but also the effective protection of tiny Au_{25} from aggregation by UiO-66. Interestingly, while the reaction gives MF as the exclusive product in the presence of Na_2CO_3, the selectivity completely turns to the acetal product in the absence of Na_2CO_3 (entry 10), the latter of which might be ascribed to the abundant Lewis acid sites in UiO-66, promoting acetal production.[55] Given that alkaline substances are able to inhibit acetal production and promote the oxidation of hemiacetals to esters,[56,57] the addition of Na_2CO_3 is necessary for the oxidative esterification reaction of furfural with methanol.

Powder XRD patterns of Au_{25}@UiO-66 and Au_{25}/UiO-66 after catalysis demonstrate the well-retained MOF crystallinity.

https://doi.org/10.1021/jacs.2c09136
J. Am. Chem. Soc. 2022, 144, 22008−22017

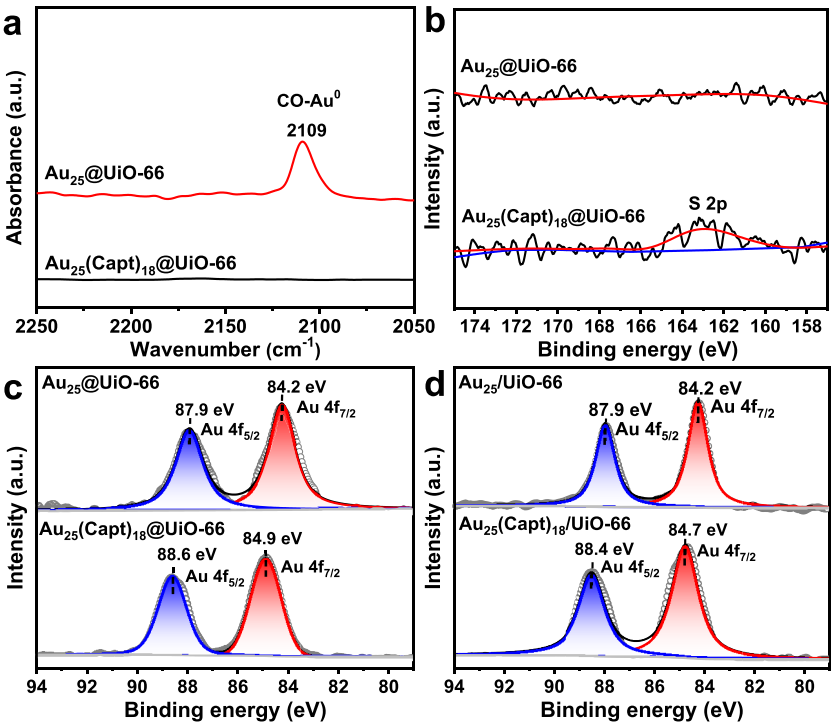

Figure 2. (a) CO-DRIFTS spectra on $Au_{25}(Capt)_{18}$@UiO-66 and Au_{25}@UiO-66 at 298 K. (b) XPS spectra of S 2p for $Au_{25}(Capt)_{18}$@UiO-66 and Au_{25}@UiO-66. XPS spectra of Au 4f for (c) $Au_{25}(Capt)_{18}$@UiO-66 and Au_{25}@UiO-66, and (d) $Au_{25}(Capt)_{18}$/UiO-66 and Au_{25}/UiO-66.

Table 1. Oxidative Esterification of Furfural with Methanol over Au_{25} NCs in Combination with UiO-66[a]

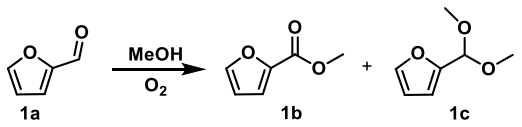

entry	catalyst	Con. (%)	Sel. 1b (%)	Sel. 1c (%)
1	UiO-66	N.D.		
2	none	N.D.		
3	$Au_{25}(Capt)_{18}$	3.5	100	N.D.[b]
4	$Au_{25}(Capt)_{18}$@UiO-66	2.8	100	N.D.
5	$Au_{25}(Capt)_{18}$/UiO-66	5.1	100	N.D.
6	Au_{25}@UiO-66	99.9	100	N.D.
7	Au_{25}/UiO-66	68.6	100	N.D.
8	Au_{25}/ZrO_2	57.9	100	N.D.
9	AuNPs@UiO-66	62.4	100	N.D.
10[c]	Au_{25}@UiO-66	99.9	N.D.	100

[a]Reaction conditions: furfural (0.1 mmol), catalyst (15 mg, ~2 wt % Au loading based on ICP results, Table S1) and Na_2CO_3 (2 mg) in 4 mL methanol under 6 bar of O_2 at 100 °C for 4 h. [b]N.D.: not detectable. [c]Without Na_2CO_3.

However, the Au diffraction peak at 38° becomes identifiable in Au_{25}/UiO-66, which is a sign of the formation of large-sized Au NPs (Figure S15). TEM images display no change of Au_{25} in Au_{25}@UiO-66 after the reaction, while significant aggregation of Au_{25} on the MOF external surface occurs to Au_{25}/UiO-66 (Figure S16), which is consistent with the observation in the powder XRD results. Au detachment up to 10.2% is found from Au_{25}/UiO-66 after reaction, while almost no leaching is detected for Au_{25}@UiO-66. These results unambiguously demonstrate that MOF encapsulation is able to inhibit aggregation and detachment of Au_{25}, accounting for the superior catalytic activity and stability of Au_{25}@UiO-66.

Given the unique advantage of MOFs on structural tailorability, a series of isoreticular UiO-66-X are readily constructed by adopting the BDC-X linker with diverse functional groups to afford Au_{25}@UiO-66-X (X = H, NH_2, OH, and NO_2), serving as an ideal platform to understand how the surrounding microenvironment of Au_{25} affects the catalysis. To exclude the effect of mass transfer resistance as much as possible, a mixed ligand approach was adopted for the synthesis of UiO-66-X to ensure their similar size and morphology. The UV−vis diffuse reflectance spectra display a clear $Au_{25}(Capt)_{18}$ characteristic peak in $Au_{25}(Capt)_{18}$@UiO-66-X (Figure S17). The same heat treatment is adopted to remove the surface ligands of Au_{25} in $Au_{25}(Capt)_{18}$@UiO-66-X. The crystallinity of the resulting Au_{25}@UiO-66-X examined by powder XRD does not show decreased intensity (Figure S18). Au_{25}@UiO-66-X shares similar morphology as observed by scanning electron microscopy (SEM) (Figure S19). The HAADF-STEM and EDS mapping results for Au_{25}@UiO-66-X support that both Au_{25} and the mixed linkers are uniformly distributed in the MOF particles (Figures S20−S22). The ^1H NMR spectra for these composites before and after heat treatment by HF digestion manifest the ~1/3 of BDC-X linkers involved in UiO-66-X and demonstrate the undisturbed X group in the MOF during the heating treatment (Figure S23). N_2 adsorption confirms that the high porosity is maintained in Au_{25}@UiO-66-X, despite slight variations in their BET surface areas caused by the diverse groups dangling on the MOF pore wall (Figure S24).

The XPS spectra of S 2p and ICP−AES results jointly suggest that the ligands on the Au_{25} surface have been completely removed (Figure S25), which is further verified by the appearance of a new vibration peak of CO adsorption related to Au^0 in the CO-DRIFTS spectra of all Au_{25}@UiO-66-X (Figure 3a). Compared with Au_{25}@UiO-66, a blue shift is observed in the CO vibration peak for Au_{25}@UiO-66-NO_2. In

https://doi.org/10.1021/jacs.2c09136
J. Am. Chem. Soc. 2022, 144, 22008−22017

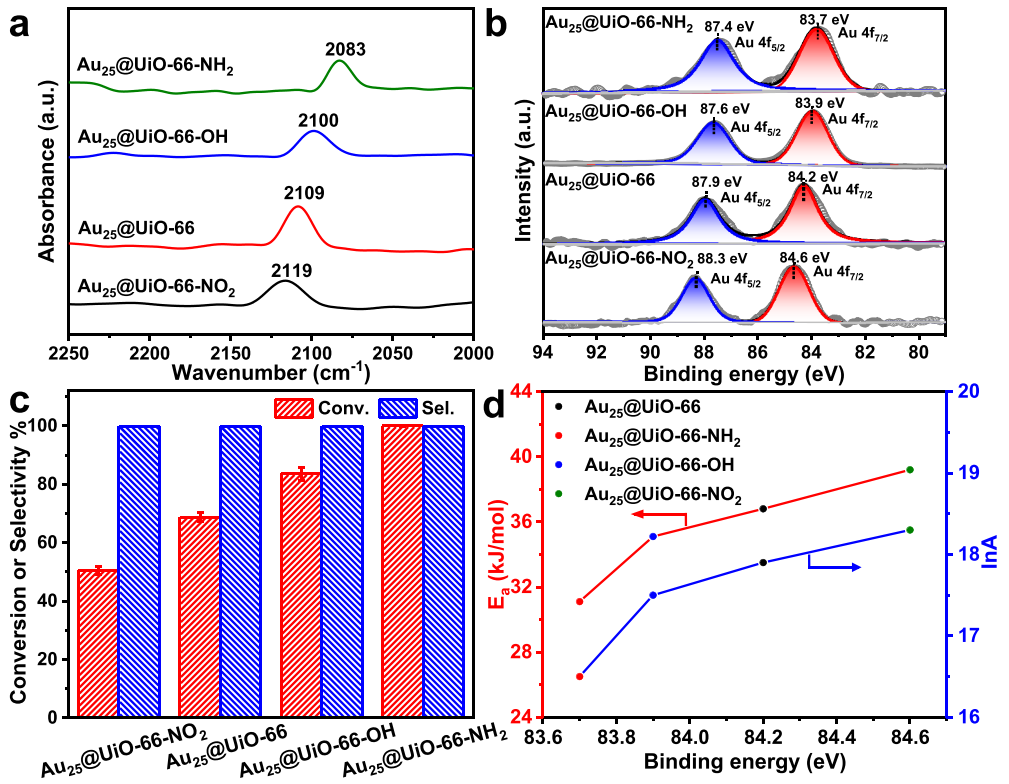

Figure 3. (a) Spectra of CO-DRIFTS on Au_{25}@UiO-66-X at 298 K. (b) XPS spectra of Au 4f for Au_{25}@UiO-66-X. (c) Activity and selectivity of Au_{25}@UiO-66-X (~2 wt % Au loading) at 100 °C for 2 h under 6 bar O_2 in the oxidative esterification of furfural. (d) Relationship between the binding energy of Au_{25} and activation energies (E_a) (the red curve guiding the eyes) and the natural logarithm of the pre-exponential factor (ln A) (the blue curve guiding the eyes) of Au_{25}@UiO-66-X in the oxidative esterification of furfural with methanol.

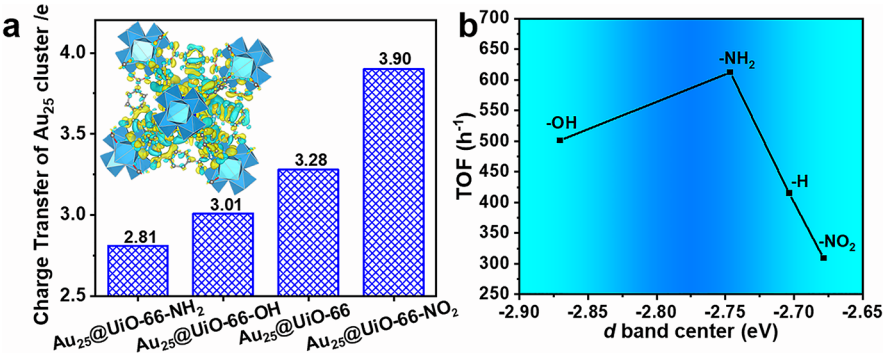

Figure 4. (a) Calculated number of electron transfer from Au_{25} to the host MOF in Au_{25}@UiO-66-X (inset: electron density distribution of Au_{25}@UiO-66-NH_2 as a representative). (b) Relationship between the d-band center and catalytic activity (TOF).

contrast, red shifts occur for Au_{25}@UiO-66-NH_2 and Au_{25}@UiO-66-OH, the latter of which gives a larger shift. Since the peak position of CO adsorption is directly related to the Au electronic state, a lower wavenumber is correlated to a higher Au electron density.[50] Accordingly, the electron density on Au_{25} follows the trend of Au_{25}@UiO-66-NH_2 > Au_{25}@UiO-66-OH > Au_{25}@UiO-66 > Au_{25}@UiO-66-NO_2, which is further supported by the binding energy difference in Au 4f peaks of XPS spectra (Figure 3b). Taking together, the discriminated microenvironment induced by MOF pore wall engineering effectively regulates the electronic state of encapsulated Au_{25}.

Encouraged by the regulated Au_{25} electronic states, the catalytic performance of Au_{25}@UiO-66-X with the same amount (~2 wt % of Au loading, Table S1) and spatial location of Au_{25} has been then examined in the oxidative esterification of furfural. It is interesting to note that, despite sharing comparable active sites and structures, the catalytic activities of Au_{25}@UiO-66-X are distinctly different. Remarkably, Au_{25}@UiO-66-NH_2 features the best catalytic activity and accomplishes the conversion within 2 h (Figure 3c). By comparison, the conversions of Au_{25}@UiO-66-OH, Au_{25}@UiO-66, and Au_{25}@UiO-66-NO_2 are 83.6, 68.7, and 51.8%, respectively, although all these catalysts give exclusive selectivity to MF. The apparent activation energies (E_a) and the natural logarithm of the pre-exponential factor (ln A) are estimated based on the Arrhenius relationship. The E_a of Au_{25}@UiO-66-NH_2, Au_{25}@UiO-66-OH, Au_{25}@UiO-66, and Au_{25}@UiO-66-NO_2 determined by kinetic experiments are 31.1, 35.1, 36.8, and 39.2 kJ/mol, respectively (Figure S26), well corresponding to the reverse sequence of activity (the

https://doi.org/10.1021/jacs.2c09136
J. Am. Chem. Soc. 2022, 144, 22008−22017

higher E_a, the lower activity). The relationship between E_a and ln A and the binding energy of Au_{25} can be established (Figure 3d). Both E_a and ln A are positively correlated with the binding energy of Au_{25}, which further supports that the activity of Au_{25} decreases with the increased electron-withdrawing effect of the functional groups on the pore wall. After the catalytic process, the MOF crystallinity and highly dispersed feature of Au_{25} NCs are well maintained in all catalysts, as evidenced by powder XRD patterns and HAADF-STEM images (Figures S27 and S28).

To gain more insights into the influence on the electronic state and catalytic activity of Au_{25} NCs by the MOF pore wall engineering, density functional theory (DFT) calculations have been adopted to evaluate the Bader charge and d-band center of these catalysts. The geometries of Au_{25} in Au_{25}@UiO-66-X are optimized by the Vienna ab initio simulation package (VASP).[58] Based on the optimized model of Au_{25}@UiO-66-X (Figure S29), the number of electrons transferred from Au_{25} to UiO-66-NH_2, UiO-66-OH, UiO-66, and UiO-66-NO_2 is calculated to be 2.81, 3.01, 3.28, and 3.90 e, respectively (Figure 4a). The degree of Au_{25} electron donation is in the order of Au_{25}@UiO-66-NO_2 > Au_{25}@UiO-66 > Au_{25}@UiO-66-OH > Au_{25}@UiO-66-NH_2, in agreement with the above CO-DRIFTS and XPS results. It is evident that electron transfer occurs mainly in the region between Au_{25} and UiO-66-X linkers in the charge distribution diagram (Figure S30), illuminating that the electron-withdrawing and -donating effect of the MOF groups regulates the extent of electron transfer from Au_{25} to UiO-66-X. The degree of electron donation of Au_{25} fits well with the trend of their activity, illustrating that the charge transfer between Au_{25} and the host MOFs plays a critical role in the resulting activity.

Furthermore, the d-band center has been calculated for the Au_{25} encapsulated by UiO-66-X. The approximate location of the d-band center of Au_{25} is −2.87, −2.75, −2.70, and −2.68 eV for Au_{25}@UiO-66-OH, Au_{25}@UiO-66-NH_2, Au_{25}@UiO-66, and Au_{25}@UiO-66-NO_2, respectively. The relationship between the d-band center position of the Au_{25} and their catalytic activity (TOF value) for Au_{25}@UiO-66-X presents a volcano-type trend, in which Au_{25}@UiO-66-NH_2 with a moderate d-band center exhibits the highest activity (Figure 4b). According to the d-band center theory, the closer the d-band center is to the Fermi energy level, the stronger the adsorption ability of the catalyst to the substrate.[59] As a result, the order of substrate adsorption ability is Au_{25}@UiO-66-NO_2 > Au_{25}@UiO-66 > Au_{25}@UiO-66-NH_2 > Au_{25}@UiO-66-OH. The classical Sabatier principle suggests that the strength of substrate adsorption on the catalyst determines the catalytic activity; moderate strength is favorable to the reaction, while too strong or too weak strength will reduce the catalytic ability,[60,61] in which the moderate substrate adsorption intensity of Au_{25}@UiO-66-NH_2 accounts for its highest activity.

The stability and recyclability of Au_{25}@UiO-66-NH_2 are investigated. No noticeable decrease in activity or selectivity is observed in the consecutive five cycles (Figure S31). Powder XRD patterns and TEM images demonstrate that the catalyst microstructure is retained after five runs of reaction (Figures S32 and S33). Moreover, the catalyst is filtered out after 1 h of reaction; the results show that no further product is harvested under the same conditions (Figure S34), inferring that no leaching of Au_{25} occurred and the process should be truly heterogeneous. In addition, different furfural derivatives have been examined over Au_{25}@UiO-66-NH_2. The reaction of diverse furfural derivatives in methanol produces the corresponding methyl esters in excellent yields (Table S2). It is worth noting that 5-hydroxymethylfurfural can be efficiently transformed to furan-2,5-dimethylmethanoate, which is the essential polymer monomer and a renewable platform chemical (entry 6).[51]

CONCLUSIONS

In summary, the $Au_{25}(Capt)_{18}$ NCs have been encapsulated into UiO-66, followed by the removal of the surface ligand on Au_{25} to afford surface-clean Au_{25}@UiO-66 by taking advantage of the confinement effect of the MOF. Thanks to the uniform and tiny size as well as the fully exposed active sites of ligand-free Au_{25} protected by the MOF with good resistance to aggregation, the Au_{25}@UiO-66 exhibits its excellent performance in the catalytic oxidative esterification of furfural, a critical process in fine chemicals. Upon the integration of ligand-free Au_{25} into UiO-66-X with diverse functional groups dangling on the pore wall, the resulting Au_{25}@UiO-66-X afford distinctly different activities, in which Au_{25}@UiO-66-NH_2 possesses the best activity and gives excellent conversions toward diverse furfural derivatives. Experiments and DFT calculations jointly unveil that the modulated microenvironment around Au_{25} sites created by pore wall engineering of the MOFs regulates the Au electron state and substrate adsorption strength on Au_{25} sites, which dominate the catalytic performance. This work unprecedentedly introduces surface-clean metal NCs into isoreticular MOFs, which not only integrates the respective merits of each component but also creates a modulated microenvironment for active metal clusters, opening a door to the fabrication of supported catalysts with precise and tailorable structures for enhanced catalysis.

EXPERIMENTAL SECTION

Synthesis of $Au_{25}(Capt)_{18}$ NCs. $Au_{25}(Capt)_{18}$ was synthesized via a size-focusing strategy according to the previous report with some modifications.[42] First, tetraoctylammonium bromide (82.8 mg) was dissolved into 5.4 mL of $HAuCl_4 \cdot 4H_2O$ methanol solution (10 mg/mL) and stirred vigorously at room temperature for 20 min; the solution color changed from yellow-orange to deep red. Then, 3.5 mL of Capt methanol solution (41.2 mg/mL) was added to the above solution, and the color quickly changed to white. After stirring for 30 min, 3.25 mL of $NaBH_4$ cold water solution (15.2 mg/mL) was added to the reaction system, and the color directly changed to brown-black. After the etching process for 8 h, the reaction solution was centrifuged to remove the unreacted, insoluble substance. The supernatant was collected and concentrated by rotary evaporation. The $Au_{25}(Capt)_{18}$ products were collected and washed thoroughly with acetonitrile−water (v/v = 3:1), and then, the black powder was obtained by vacuum drying at room temperature.

Synthesis of UiO-66. UiO-66 was synthesized according to the previous report with some modifications.[43] First, 70% of zirconium propoxide [$Zr(OnPr)_4$] solution (1.42 mL), DMF (140 mL), and CH_3COOH (80 mL) were added into a 300 mL pressure vial and heated in an oven at 130 °C for 2 h. The color changed from colorless to yellow. After cooling to room temperature, we obtained solution A. Then, BDC (300 mg) was added into solution A (45 mL), sonicated for 1 min, and stirred for 24 h at 25 °C. The white precipitate was collected by centrifugation and washed with DMF and MeOH three times, respectively. Finally, the precipitate was soaked in 100 mL MeOH for 48 h and dried in vacuum at 60 °C overnight to afford UiO-66 powder.

Synthesis of $Au_{25}(Capt)_{18}$/UiO-66. Typically, 100 mg of UiO-66 was dispersed in 3 mL of MeOH under sonication, followed by adding 1.8 mL of $Au_{25}(Capt)_{18}$ methanolic solution (2 mg/mL). After

https://doi.org/10.1021/jacs.2c09136
J. Am. Chem. Soc. 2022, 144, 22008−22017

stirring for 2 h, the solution was centrifuged. The light brown precipitate was washed with MeOH and dried in vacuum at 60 °C overnight.

Synthesis of $Au_{25}(Capt)_{18}$@UiO-66. Typically, 3.2 mL of $Au_{25}(Capt)_{18}$ methanolic solution (2 mg/mL) was added into the aforementioned solution A (45 mL) by sonication for 1 min and stirred for 20 min at 25 °C. Then, 300 mg BDC was mixed with the solution, sonicated for 1 min, and stirred for 24 h at room temperature. The light brown precipitate was collected by centrifugation and washed with DMF and MeOH three times, respectively. Finally, the precipitate was soaked in 100 mL MeOH for 48 h and dried in vacuum at 60 °C overnight.

Synthesis of $Au_{25}(Capt)_{18}$@UiO-66-NH_2. Typically, 3.2 mL of $Au_{25}(Capt)_{18}$ methanolic solution (2 mg/mL) was added into the aforementioned solution A (64 mL) by sonication for 1 min and stirred for 20 min at 25 °C. Then, 163.2 mg NH_2-BDC and 150 mg BDC were mixed with the solution, sonicated for 1 min, and stirred for 24 h at room temperature. The yellowish-brown precipitate was collected by centrifugation and washed with DMF and MeOH three times, respectively. Finally, the precipitate was soaked in 100 mL MeOH for 48 h and dried in vacuum at 60 °C overnight.

Synthesis of $Au_{25}(Capt)_{18}$@UiO-66-OH. Typically, 1.92 mL of $Au_{25}(Capt)_{18}$ methanolic solution (2 mg/mL) was added into the aforementioned solution A (44 mL) by sonication for 1 min and stirred for 20 min at 25 °C. Then, OH-BDC (82.8 mg) and BDC (75 mg) were mixed with the solution, sonicated for 1 min, and stirred for 24 h at room temperature. The light brown precipitate was collected by centrifugation and washed with DMF and MeOH three times, respectively. Finally, the precipitate was soaked in 100 mL MeOH for 48 h and dried in vacuum at 60 °C overnight.

Synthesis of $Au_{25}(Capt)_{18}$@UiO-66-NO_2. Typically, 1.92 mL $Au_{25}(Capt)_{18}$ methanolic solution (2 mg/mL) was added into the aforementioned solution A (44 mL) by sonication for 1 min and stirred for 20 min at 25 °C. Then, NO_2-BDC (96 mg) and BDC (75 mg) were mixed with the solution, sonicated for 2 min, and stirred for 24 h at room temperature. The light brown precipitate was collected by centrifugation and washed with DMF and MeOH three times, respectively. Finally, the precipitate was soaked in 100 mL MeOH for 48 h and dried in vacuum at 60 °C overnight.

Synthesis of AuNPs@UiO-66. The AuNPs@UiO-66 sample was synthesized according to the reported method with minor modifications.[62] Typically, 50 mg of activated UiO-66 powder was dispersed in 10 mL of ultrapure water by ultrasonication. Then, 200 μL of aqueous $HAuCl_4$ solution (25.4 mM) was added dropwise and stirred for 4 h. The precipitate was collected by centrifugation and redispersed into 10 mL of ultrapure water. After that, 500 μL of ice-cold aqueous $NaBH_4$ solution (0.1 M) was added dropwise and stirred for another 4 h in the dark. Finally, the precipitate was collected by centrifugation, washed three times with ultrapure water, and dried in vacuum at 60 °C overnight.

Synthesis of $Au_{25}(Capt)_{18}/ZrO_2$. Typically, 1 mL $Au_{25}(Capt)_{18}$ methanol solution (2 mg/mL) was added to 50 mg ZrO_2 under vigorous stirring. After 30 min of stirring at room temperature, the brown precipitate was collected by centrifugation and dried under vacuum at 60 °C overnight.

Capt Ligand Removal from $Au_{25}(Capt)_{18}$/UiO-66, $Au_{25}(Capt)_{18}$@UiO-66-X, and $Au_{25}(Capt)_{18}/ZrO_2$ by Thermal Treatment. The composites were heated to 275 °C with a heating rate of 5 °C/min and maintained at this temperature for 3 h in vacuum. After that, the samples were cooled down to room temperature naturally.

Oxidative Esterification Reaction of Furfural with MeOH. Typically, 15 mg of catalyst (~2 wt % of Au loading, Table S1), 0.1 mmol furfural, and 2 mg Na_2CO_3 were dispersed in 4 mL of MeOH, followed by addition into a 25 mL high-pressure reactor (NSV-25-316 L, Anhui Kemi-n Instrument Co., Ltd, China). After pressurization (6 bar) with O_2, the mixture was heated to 100 °C (5 °C/min) and stirred (400 rpm). After the reaction, the reactor was cooled to room temperature, and the reaction solution was centrifuged to separate the catalyst from the solvent. The conversion and selectivity were subsequently quantified by gas chromatography (GC), and the products were confirmed by GC−MS. The TOF was calculated based on the reaction rate at 10−20% conversion of furfural and the total Au loading in the Au_{25}@UiO-66-X catalyst.

Recyclability Test of Au_{25}@UiO-66-NH_2. The catalyst was collected by centrifugation from the reacted solution, washed with MeOH three times, and dried under vacuum after each cycle. Afterward, the catalyst was reused for the next cycle under the same reaction conditions.

Oxidative Esterification Reaction of Furfural Derivatives with MeOH. Typically, 15 mg of catalyst (~2 wt % of Au loading, Table S1) powder and 2 mg of Na_2CO_3 were dispersed in 4 mL of MeOH, followed by the addition of 0.1 mmol of furfural derivatives into a 25 mL high-pressure reactor. After pressurization (6 bar) with O_2, the mixture was heated to 100 °C (5 °C/min) and stirred (400 rpm). After the reaction had taken place for a desired amount of time, the reactor was cooled down to room temperature, and the reaction solution was centrifuged to separate the catalyst from the solvent. The conversion and selectivity were subsequently quantified by GC, and the products were confirmed by GC−MS.

Characterizations. All chemicals were obtained from commercial sources and were not further purified. De-ionized water was produced through reverse osmosis (specific resistance of 18.25 MΩ·cm), followed by ion exchange and filtration (Hefei Purified Water Treatment Co., Ltd). Powder XRD patterns were recorded on a Japan Rigaku Miniflex 600 equipped with graphite monochromatized Cu Kα radiation (λ = 1.54 Å). UV−vis spectra were obtained on a Shimadzu UV-2700 spectrophotometer. The MALDI-TOF-MS spectrum was performed on an Autoflex Speed TOF/TOF, and the alpha-cyano-4-hydroxycinnamic acid was used as a matrix in the MALDI analysis. TGA was performed on SDT Q600 under a N_2 atmosphere with a heating rate of 5 °C/min. XPS measurements were recorded by using a Thermo ESCALAB 250 high-performance electron spectrometer using S2-monochromatized Al Kα as the excitation source. CO-DRIFTS was acquired on a Thermo Scientific Nicolet iS10 FTIR spectrometer equipped with an MCT detector. SEM was observed on a Zeiss Supra 40 scanning electron microscope at an acceleration voltage of 5 kV. The TEM images were obtained on JEOL-2010. The HAADF-STEM and EDS mapping analyses were performed on the Talos F200X instrument equipped with Super-X EDX operating at 200 kV. The SE-STEM and its corresponding HAADF-STEM images were obtained with a JEOL JEM-F200. N_2 sorption measurements were conducted at 77 K using the Micrometritics ASAP 2020. The content of Au was measured on a Thermo Scientific iCAP 7400 series instrument ICP−AES. ^{1}H NMR spectra were attained on a Bruker AC-400FT spectrometer (400 MHz). The catalytic reaction products were identified and quantified by GC (Shimadzu 2010 Plus, 0.25 mm × 30 m Rtx-5 capillary column) and then determined using an Agilent Technologies model 7890A gas chromatograph and an Agilent Technologies model 5975C mass spectrometer as the detector.

Calculation Details. The electronic structure calculations are performed using the Vienna Ab-initio Simulation Package (VASP5.4.1) within the Perdew−Burke−Ernzerhof functional and projector augmented wave potentials, which has been proved to be a suitable method for the system of MOFs.[63] A 1 × 1 × 1 Γ-centered k-point and 450 eV cutoff energy were adopted to obtain accurate electronic energy in ground-state. The convergence standards of energy and force were selected as 10^{-6} eV and 0.05 eV/Å. The position of the center of the d-band states (ε_d) of Au_{25} encapsulated in different UiO-66-X (X = H, NH_2, OH, NO_2) skeletons was calculated as follows[59]

$$\varepsilon_d = \frac{\int_{-\infty}^{+\infty} E \cdot D(E)\, dE}{\int_{-\infty}^{+\infty} D(E)\, dE}$$

where $D(E)$ is the density of d-states function of the Au atoms and E is the energy relative to the Fermi level.

https://doi.org/10.1021/jacs.2c09136
J. Am. Chem. Soc. 2022, 144, 22008−22017

■ ASSOCIATED CONTENT

Supporting Information

The Supporting Information is available free of charge at https://pubs.acs.org/doi/10.1021/jacs.2c09136.

Additional characterizations of materials, computational details, and catalytic results (PDF)

■ AUTHOR INFORMATION

Corresponding Author

Hai-Long Jiang − *Department of Chemistry, University of Science and Technology of China, Hefei, Anhui 230026, P. R. China;* orcid.org/0000-0002-2975-7977; Email: jianglab@ustc.edu.cn

Authors

He Wang − *Department of Chemistry, University of Science and Technology of China, Hefei, Anhui 230026, P. R. China*

Xiyuan Liu − *Department of Chemistry, University of Science and Technology of China, Hefei, Anhui 230026, P. R. China*

Weijie Yang − *Department of Power Engineering, School of Energy, Power and Mechanical Engineering, North China Electric Power University, Baoding, Hebei 071003, P. R. China;* orcid.org/0000-0002-0232-1129

Guangyang Mao − *Department of Power Engineering, School of Energy, Power and Mechanical Engineering, North China Electric Power University, Baoding, Hebei 071003, P. R. China*

Zheng Meng − *Department of Chemistry, University of Science and Technology of China, Hefei, Anhui 230026, P. R. China*

Zhikun Wu − *Key Laboratory of Materials Physics, Anhui Key Laboratory of Nanomaterials and Nanotechnology, CAS Center for Excellence in Nanoscience, Institute of Solid State Physics, HIPS, Chinese Academy of Sciences, Hefei, Anhui 230031, P. R. China;* orcid.org/0000-0002-2711-3860

Complete contact information is available at: https://pubs.acs.org/10.1021/jacs.2c09136

Notes

The authors declare no competing financial interest.

■ ACKNOWLEDGMENTS

This work was supported by the National Key Research and Development Program of China (2021YFA1500402), the National Natural Science Foundation of China (21725101, 22161142001 and 21871244), Collaborative Innovation Program of Hefei Science Center, CAS (2020HSC-CIP005), and the Fundamental Research Funds for the Central Universities (WK3450000007 and WK2060000038).

■ REFERENCES

(1) Munnik, P.; de Jongh, P. E.; de Jong, K. P. Recent developments in the synthesis of supported catalysts. *Chem. Rev.* **2015**, *115*, 6687−6718.

(2) Sankar, M.; He, Q.; Engel, R. V.; Sainna, M. A.; Logsdail, A. J.; Roldan, A.; Willock, D. J.; Agarwal, N.; Kiely, C. J.; Hutchings, G. J. Role of the support in gold-containing nanoparticles as heterogeneous catalysts. *Chem. Rev.* **2020**, *120*, 3890−3938.

(3) Zhang, L.; Zhou, M.; Wang, A.; Zhang, T. Selective hydrogenation over supported metal catalysts: from nanoparticles to single atoms. *Chem. Rev.* **2020**, *120*, 683−733.

(4) Jin, R.; Zeng, C.; Zhou, M.; Chen, Y. Atomically precise colloidal metal nanoclusters and nanoparticles: fundamentals and opportunities. *Chem. Rev.* **2016**, *116*, 10346−10413.

(5) Takano, S.; Tsukuda, T. Chemically modified gold/silver superatoms as artificial elements at nanoscale: Design principles and synthesis challenges. *J. Am. Chem. Soc.* **2021**, *143*, 1683−1698.

(6) Jin, Y.; Zhang, C.; Dong, X. Y.; Zang, S. Q.; Mak, T. C. W. Shell engineering to achieve modification and assembly of atomically-precise silver clusters. *Chem. Soc. Rev.* **2021**, *50*, 2297−2319.

(7) Du, Y.; Sheng, H.; Astruc, D.; Zhu, M. Atomically precise noble metal nanoclusters as efficient catalysts: a bridge between structure and properties. *Chem. Rev.* **2020**, *120*, 526−622.

(8) Jin, R.; Li, G.; Sharma, S.; Li, Y.; Du, X. Toward active-site tailoring in heterogeneous catalysis by atomically precise metal nanoclusters with crystallographic structures. *Chem. Rev.* **2021**, *121*, 567−648.

(9) Fang, J.; Zhang, B.; Yao, Q.; Yang, Y.; Xie, J.; Yan, N. Recent advances in the synthesis and catalytic applications of ligand-protected, atomically precise metal nanoclusters. *Coord. Chem. Rev.* **2016**, *322*, 1−29.

(10) Hu, C.; Chen, R.; Zheng, N. Chemical insights into interfacial effects in inorganic nanomaterials. *Adv. Mater.* **2021**, *33*, 2006159.

(11) Luo, L.; Jin, R. Atomically precise metal nanoclusters meet metal-organic frameworks. *iScience* **2021**, *24*, 103206.

(12) Masuda, S.; Takano, S.; Yamazoe, S.; Tsukuda, T. Synthesis of active, robust and cationic Au_{25} cluster catalysts on double metal hydroxide by long-term oxidative aging of $Au_{25}(SR)_{18}$. *Nanoscale* **2022**, *14*, 3031−3039.

(13) Kawawaki, T.; Kataoka, Y.; Hirata, M.; Akinaga, Y.; Takahata, R.; Wakamatsu, K.; Fujiki, Y.; Kataoka, M.; Kikkawa, S.; Alotabi, A. S.; Hossain, S.; Osborn, D. J.; Teranishi, T.; Andersson, G. G.; Metha, G. F.; Yamazoe, S.; Negishi, Y. Creation of high-performance heterogeneous photocatalysts by controlling ligand desorption and particle size of gold nanocluster. *Angew. Chem., Int. Ed.* **2021**, *60*, 21340−21350.

(14) Pollitt, S.; Truttmann, V.; Haunold, T.; Garcia, C.; Olszewski, W.; Llorca, J.; Barrabés, N.; Rupprechter, G. The dynamic structure of $Au_{38}(SR)_{24}$ nanoclusters supported on CeO_2 upon pretreatment and CO oxidation. *ACS Catal.* **2020**, *10*, 6144−6148.

(15) Qin, R.; Liu, K.; Wu, Q.; Zheng, N. Surface coordination chemistry of atomically dispersed metal catalysts. *Chem. Rev.* **2020**, *120*, 11810−11899.

(16) Wang, Y.; Wan, X. K.; Ren, L.; Su, H.; Li, G.; Malola, S.; Lin, S.; Tang, Z.; Häkkinen, H.; Teo, B. K.; Wang, Q. M.; Zheng, N. Atomically precise alkynyl-protected metal nanoclusters as a model catalyst: Observation of promoting effect of surface ligands on catalysis by metal nanoparticles. *J. Am. Chem. Soc.* **2016**, *138*, 3278−3281.

(17) Wan, X.-K.; Wang, J.-Q.; Nan, Z.-A.; Wang, Q.-M. Ligand effects in catalysis by atomically precise gold nanoclusters. *Sci. Adv.* **2017**, *3*, 1701823.

(18) Cirri, A.; Morales Hernández, H.; Kmiotek, C.; Johnson, C. J. Systematically tuning the electronic structure of gold nanoclusters through ligand derivatization. *Angew. Chem., Int. Ed.* **2019**, *58*, 13818−13822.

(19) Furukawa, H.; Cordova, K. E.; O'Keeffe, M.; Yaghi, O. M. The chemistry and applications of metal-organic frameworks. *Science* **2013**, *341*, 1230444.

(20) Zhou, H.-C.; Kitagawa, S. Metal−organic frameworks (MOFs). *Chem. Soc. Rev.* **2014**, *43*, 5415−5418.

(21) Zhao, X.; Wang, Y.; Li, D.-S.; Bu, X.; Feng, P. Metal−organic frameworks for separation. *Adv. Mater.* **2018**, *30*, 1705189.

(22) Lin, R.-B.; Zhang, Z.; Chen, B. Achieving high performance metal−organic framework materials through pore engineering. *Acc. Chem. Res.* **2021**, *54*, 3362−3376.

(23) Yang, Q.; Xu, Q.; Jiang, H. L. Metal−organic frameworks meet metal nanoparticles: synergistic effect for enhanced catalysis. *Chem. Soc. Rev.* **2017**, *46*, 4774−4808.

(24) Fang, C.; Liu, L.; Weng, J.; Zhang, S.; Zhang, X.; Ren, Z.; Shen, Y.; Meng, F.; Zheng, B.; Li, S.; Wu, J.; Shi, W.; Lee, S.; Zhang, W.; Huo, F. Modifiers versus channels: creating shape-selective catalysis of

metal nanoparticles/porous nanomaterials. *Angew. Chem., Int. Ed.* **2021**, *60*, 976−982.
(25) Choi, K. M.; Na, K.; Somorjai, G. A.; Yaghi, O. M. Chemical environment control and enhanced catalytic performance of platinum nanoparticles embedded in nanocrystalline metal−organic frameworks. *J. Am. Chem. Soc.* **2015**, *137*, 7810−7816.
(26) Aijaz, A.; Karkamkar, A.; Choi, Y. J.; Tsumori, N.; Rönnebro, E.; Autrey, T.; Shioyama, H.; Xu, Q. Immobilizing highly catalytically active Pt nanoparticles inside the pores of metal−organic framework: a double solvents approach. *J. Am. Chem. Soc.* **2012**, *134*, 13926−13929.
(27) Li, X.; Goh, T. W.; Li, L.; Xiao, C.; Guo, Z.; Zeng, X. C.; Huang, W. Controlling catalytic properties of Pd nanoclusters through their chemical environment at the atomic level using isoreticular metal−organic frameworks. *ACS Catal.* **2016**, *6*, 3461−3468.
(28) Chen, F.; Shen, K.; Chen, J.; Yang, X.; Cui, J.; Li, Y. General immobilization of ultrafine alloyed nanoparticles within metal−organic frameworks with high loadings for advanced synergetic catalysis. *ACS Cent. Sci.* **2019**, *5*, 176−185.
(29) Li, G.; Zhao, S.; Zhang, Y.; Tang, Z. Metal−organic frameworks encapsulating active nanoparticles as emerging composites for catalysis: recent progress and perspectives. *Adv. Mater.* **2018**, *30*, 1800702.
(30) Chen, Y. Z.; Wang, Z. U.; Wang, H.; Lu, J.; Yu, S. H.; Jiang, H. L. Singlet oxygen-engaged selective photo-oxidation over Pt nanocrystals/porphyrinic MOF: the roles of photothermal effect and Pt electronic state. *J. Am. Chem. Soc.* **2017**, *139*, 2035−2044.
(31) Xu, M.; Li, D.; Sun, K.; Jiao, L.; Xie, C.; Ding, C.; Jiang, H. L. Interfacial microenvironment modulation boosting electron transfer between metal nanoparticles and MOFs for enhanced photocatalysis. *Angew. Chem., Int. Ed.* **2021**, *60*, 16372−16376.
(32) Kratzl, K.; Kratky, T.; Günther, S.; Tomanec, O.; Zbořil, R.; Michalička, J.; Macak, J. M.; Cokoja, M.; Fischer, R. A. Generation and stabilization of small platinum clusters $Pt_{12\pm x}$ inside a metal−organic framework. *J. Am. Chem. Soc.* **2019**, *141*, 13962−13969.
(33) Luo, Y.; Fan, S.; Yu, W.; Wu, Z.; Cullen, D. A.; Liang, C.; Shi, J.; Su, C. Fabrication of $Au_{25}(SG)_{18}$-ZIF-8 nanocomposites: a facile strategy to position $Au_{25}(SG)_{18}$ nanoclusters inside and outside ZIF-8. *Adv. Mater.* **2018**, *30*, 1704576.
(34) Yun, Y.; Sheng, H.; Bao, K.; Xu, L.; Zhang, Y.; Astruc, D.; Zhu, M. Design and remarkable efficiency of the robust sandwich cluster composite nanocatalysts ZIF-8@Au_{25}@ZIF-67. *J. Am. Chem. Soc.* **2020**, *142*, 4126−4130.
(35) Zhao, Y.; Zhuang, S.; Liao, L.; Wang, C.; Xia, N.; Gan, Z.; Gu, W.; Li, J.; Deng, H.; Wu, Z. A dual purpose strategy to endow gold nanoclusters with both catalysis activity and water solubility. *J. Am. Chem. Soc.* **2020**, *142*, 973−977.
(36) Chu, K.; Luo, Y.; Wu, D.; Su, Z.; Shi, J.; Zhang, J. Z.; Su, C. Y. Charge state of $Au_{25}(SG)_{18}$ nanoclusters induced by interaction with a metal organic framework support and its effect on catalytic performance. *J. Phys. Chem. Lett.* **2021**, *12*, 8003−8008.
(37) Yun, Y.; Fang, Y.; Fu, W.; Du, W.; Zhu, Y.; Sheng, H.; Astruc, D.; Zhu, M. Exploiting the fracture in metal-organic frameworks: a general strategy for bifunctional atom-precise nanocluster/ZIF-8 (300 °C) composites. *Small* **2022**, *18*, 2107459.
(38) Li, L.; Li, Z.; Yang, W.; Huang, Y.; Huang, G.; Guan, Q.; Dong, Y.; Lu, J.; Yu, S.-H.; Jiang, H.-L. Integration of Pd nanoparticles with engineered pore walls in MOFs for enhanced catalysis. *Chem* **2021**, *7*, 686−698.
(39) Chen, D.; Yang, W.; Jiao, L.; Li, L.; Yu, S. H.; Jiang, H. L. Boosting catalysis of Pd nanoparticles in MOFs by pore wall engineering: the roles of electron transfer and adsorption energy. *Adv. Mater.* **2020**, *32*, 2000041.
(40) Li, J.; Huang, H.; Xue, W.; Sun, K.; Song, X.; Wu, C.; Nie, L.; Li, Y.; Liu, C.; Pan, Y.; Jiang, H.-L.; Mei, D.; Zhong, C. Self-adaptive dual-metal-site pairs in metal-organic frameworks for selective CO_2 photoreduction to CH_4. *Nat. Catal.* **2021**, *4*, 719−729.
(41) Jiao, L.; Wang, J.; Jiang, H.-L. Microenvironment modulation in metal−organic framework-based catalysis. *Acc. Mater. Res.* **2021**, *2*, 327−339.
(42) Kumar, S.; Jin, R. Water-soluble $Au_{25}(Capt)_{18}$ nanoclusters: synthesis, thermal stability, and optical properties. *Nanoscale* **2012**, *4*, 4222−4227.
(43) DeStefano, M. R.; Islamoglu, T.; Garibay, S. J.; Hupp, J. T.; Farha, O. K. Room-temperature synthesis of UiO-66 and thermal modulation of densities of defect sites. *Chem. Mater.* **2017**, *29*, 1357−1361.
(44) Zhu, Y. F.; Qiu, X. Y.; Zhao, S. L.; Guo, J.; Zhang, X. F.; Zhao, W. S.; Shi, Y. A.; Tang, Z. Y. Structure regulated catalytic performance of gold nanocluster-MOF nanocomposites. *Nano Res.* **2020**, *13*, 1928−1932.
(45) Yoskamtorn, T.; Yamazoe, S.; Takahata, R.; Nishigaki, J.-i.; Thivasasith, A.; Limtrakul, J.; Tsukuda, T. Thiolate-mediated selectivity control in aerobic alcohol oxidation by porous carbon-supported Au_{25} clusters. *ACS Catal.* **2014**, *4*, 3696−3700.
(46) Wu, Z.; Jiang, D. E.; Mann, A. K.; Mullins, D. R.; Qiao, Z. A.; Allard, L. F.; Zeng, C.; Jin, R.; Overbury, S. H. Thiolate Ligands as a double-edged sword for CO oxidation on CeO_2 supported $Au_{25}(SCH_2CH_2Ph)_{18}$ nanoclusters. *J. Am. Chem. Soc.* **2014**, *136*, 6111−6122.
(47) Xie, S.; Tsunoyama, H.; Kurashige, W.; Negishi, Y.; Tsukuda, T. Enhancement in Aerobic Alcohol Oxidation Catalysis of Au_{25} Clusters by Single Pd Atom Doping. *ACS Catal.* **2012**, *2*, 1519−1523.
(48) Negishi, Y.; Matsuura, Y.; Tomizawa, R.; Kurashige, W.; Niihori, Y.; Takayama, T.; Iwase, A.; Kudo, A. Controlled Loading of Small Au_n Clusters (n = 10−39) onto $BaLa_4Ti_4O_{15}$ Photocatalysts: Toward an Understanding of Size Effect of Cocatalyst on Water-Splitting Photocatalytic Activity. *J. Phys. Chem. C* **2015**, *119*, 11224−11232.
(49) Feng, L.; Wang, K.-Y.; Day, G. S.; Ryder, M. R.; Zhou, H.-C. Destruction of metal−organic frameworks: positive and negative aspects of stability and lability. *Chem. Rev.* **2020**, *120*, 13087−13133.
(50) Mihaylov, M.; Knözinger, H.; Hadjiivanov, K.; Gates, B. C. Characterization of the oxidation states of supported gold species by IR spectroscopy of adsorbed CO. *Chem. Ing. Tech.* **2007**, *79*, 795−806.
(51) Fang, A.; Dhakshinamoorthy, Y.; Li, H.; Garcia, H. Metal organic frameworks for biomass conversion. *Chem. Soc. Rev.* **2020**, *49*, 3638−3687.
(52) Zhao, X.; Wang, F.; Kong, X. P.; Fang, R.; Li, Y. Dual-metal hetero-single-atoms with different coordination for efficient synergistic catalysis. *J. Am. Chem. Soc.* **2021**, *143*, 16068−16077.
(53) Wittstock, A.; Zielasek, V.; Biener, J.; Friend, C. M.; Bäumer, M. Nanoporous gold catalysts for selective gas-phase oxidative coupling of methanol at low temperature. *Science* **2010**, *327*, 319−322.
(54) Ning, L.; Liao, S.; Liu, X.; Guo, P.; Zhang, Z.; Zhang, H.; Tong, X. A regulatable oxidative valorization of furfural with aliphatic alcohols catalyzed by functionalized metal-organic frameworks-supported Au nanoparticles. *J. Catal.* **2018**, *364*, 1−13.
(55) Li, X.; Guo, Z.; Xiao, C.; Goh, T. W.; Tesfagaber, D.; Huang, W. Tandem catalysis by palladium nanoclusters encapsulated in metal−organic frameworks. *ACS Catal.* **2014**, *4*, 3490−3497.
(56) Zhao, X.; Wang, F.; Kong, X.; Fang, R.; Li, Y. Subnanometric Cu clusters on atomically Fe-doped MoO_2 for furfural upgrading to aviation biofuels. *Nat. Commun.* **2022**, *13*, 2591.
(57) Mannel, D. S.; King, J.; Preger, Y.; Ahmed, M. S.; Root, T. W.; Stahl, S. S. Mechanistic insights into aerobic oxidative methyl esterification of primary alcohols with heterogeneous PdBiTe catalysts. *ACS Catal.* **2018**, *8*, 1038−1047.
(58) Kresse, G.; Furthmüller, J. Efficient iterative schemes for ab initio total-energy calculations using a plane-wave basis set. *Phys. Rev. B* **1996**, *54*, 11169−11186.
(59) Hammer, B.; Norskov, J. K. Why gold is the noblest of all the metals. *Nature* **1995**, *376*, 238−240.

(60) Roduner, E. Understanding catalysis. *Chem. Soc. Rev.* **2014**, *43*, 8226−8239.
(61) Sun, Y.; Wang, E.; Ren, Y.; Xiao, K.; Liu, X.; Yang, D.; Gao, Y.; Ding, W.; Zhu, Y. The evolution in catalytic activity driven by periodic transformation in theinner sites of gold clusters. *Adv. Funct. Mater.* **2019**, *29*, 1904242.
(62) Chen, L.-W.; Hao, Y.-C.; Guo, Y.; Zhang, Q.; Li, J.; Gao, W.-Y.; Ren, L.; Su, X.; Hu, L.; Zhang, N.; Li, S.; Feng, X.; Gu, L.; Zhang, Y.-W.; Yin, A.-X.; Wang, B. Metal−organic framework membranes encapsulating gold nanoparticles for direct plasmonic photocatalytic nitrogen fixation. *J. Am. Chem. Soc.* **2021**, *143*, 5727−5736.
(63) Tian, Z.; Chen, D.-L.; He, T.; Yang, P.; Wang, F.-F.; Zhong, Y.; Zhu, W. Theoretical evidence on the confinement effect of Pt@UiO-66-NH_2 for cinnamaldehyde hydrogenation. *J. Phys. Chem. C* **2019**, *123*, 22114−22122.

https://doi.org/10.1021/jacs.2c09136
J. Am. Chem. Soc. 2022, 144, 22008−22017